

## Full length article

# Partial recrystallization of gum metal to achieve enhanced strength and ductility

J.-L. Zhang <sup>a,b</sup>, C.C. Tasan <sup>b,\*</sup>, M.J. Lai <sup>a</sup>, D. Yan <sup>a</sup>, D. Raabe <sup>a</sup><sup>a</sup> Max-Planck-Institut für Eisenforschung, Max-Planck-Straße 1, 40237, Düsseldorf, Germany<sup>b</sup> Department of Materials Science and Engineering, Massachusetts Institute of Technology, 77 Massachusetts Avenue, Cambridge, MA, 02139, USA

## ARTICLE INFO

## Article history:

Received 6 February 2017

Received in revised form

22 June 2017

Accepted 24 June 2017

Available online 26 June 2017

## Keywords:

Gum metal

Partial recrystallization

Microstructure heterogeneity

 $\omega$ -Phase

Dislocation channeling

## ABSTRACT

Here we present a microstructure design approach which leads to partial recrystallization and nano-precipitation within the same single-step heat treatment. This produces a dual-constituent microstructure in Ti-Nb based gum metal, which consists of nano- $\omega$ -particle-rich ultrafine recrystallized grain chains embedded in  $\omega$ -lean subgrain-containing recovered zones. This partially recrystallized microstructure exhibits an improved strength-ductility combination that surpasses the inverse strength-ductility relationship exhibited by materials with similar composition. The strengthening effects due to precipitates and grain refinement were studied by nanoindentation. The deformation mechanisms of the partially recrystallized material were investigated by in-situ scanning electron microscope tensile tests, micro-strain mapping and post-mortem microstructure characterization. The improved mechanical properties are attributed to the high yield strength of the recrystallized grains and the sequential activation of dislocation slip and dislocation channeling.

© 2017 Acta Materialia Inc. Published by Elsevier Ltd. All rights reserved.

## 1. Introduction

Partial recrystallization has been widely used as a tool to improve either the ductility or the strength of metallic materials. Typical examples of the former effect are low temperature annealing of nanostructured materials [1–3] and texture modification of Mg-alloys containing rare earth elements [4,5]. Regarding the latter effect, recrystallization is known to drastically decrease the strength of pre-strained materials [6,7]. Thus, various methods based on partial recrystallization have been studied to preserve the strength, such as post-recrystallization aging to form precipitates [8,9] and stacking fault energy reduction to retain nano-twins in the non-recrystallized zones [10,11]. Here, we propose an approach to achieve an enhanced strength-ductility combination by incorporating nano-precipitation in partial recrystallization with a single-step heat treatment. After the heat treatment of a strongly cold worked microstructure, the recrystallized and recovered constituents in the obtained microstructure are expected to have different strengthening and deformation mechanisms. This is due to the spatially differing recrystallization kinetics leading to variations in grain size

and nano-phase content. This approach is demonstrated on gum metal [12], which is a metastable  $\beta$  (bcc)-structured Ti-Nb based alloy that forms nano-sized martensitic  $\alpha''$ - or  $\omega$ -phase depending on the thermomechanical treatments. Gum metal provides the possibilities of (i) tailoring the starting microstructure guided by thorough studies on its cold worked microstructures [13,14], and (ii) introducing multiple nano-structured features ( $\alpha''$ - and  $\omega$ -phase) [15–18]. Although gum metal is a biomedical candidate alloy due to its biocompatibility and low Young's modulus (40 GPa) [12,19,20], its yield strength and its fracture resistance must be improved for biomedical applications [20–22]. These two requirements are addressed with the proposed approach.

## 2. Experimental methodology

### 2.1. Recrystallization treatment design

Gum metal was 80% cold rolled leading to deformation-induced microstructural features including elongated grains and shear bands, fiber-type crystallographic texture, and in-grain dislocation substructures. This pre-straining level with a true strain<sup>1</sup> of ~1.6

\* Corresponding author.

E-mail address: [tasan@mit.edu](mailto:tasan@mit.edu) (C.C. Tasan).<sup>1</sup> This is calculated from  $\ln(t_0/t_f)$ , where  $t$  is the rolled metal sheet thickness.

(medium deformation) provides sufficient driving force for recrystallization, and it conserves the freedom to control the recrystallization volume fraction as well. Partial recrystallization was realized at 800 °C (above the  $\beta$ -transus), based on the results of previous recrystallization studies [23–25] to avoid concurrent recrystallization and  $\alpha$ -phase formation. The presence of  $\alpha$ -phase can lead to undesired changes in the Young's modulus and work hardening rate of gum metal [12]. 50 K s<sup>-1</sup> was used as the heating rate to ensure temperature homogeneity and to suppress recovery by narrowing its time window before recrystallization.<sup>2</sup> A moderate cooling rate of -50 K s<sup>-1</sup> was selected to favor nano- $\omega$  precipitation, which is beneficial due to the associated precipitation hardening effect and dislocation channeling mechanism [26], by avoiding both  $\alpha$ -phase and martensitic  $\alpha''$ -phase transformation. The former is a diffusional transformation enhanced by slow cooling rates [25,27], whereas the latter was reported to form instead of  $\omega$  during fast cooling [28]. Fast cooling leaves a very limited time for  $\omega$ -phase transformation before the temperature reaches the  $\alpha''$ -phase transformation start temperature (~room temperature (RT)) [28,29]. Even though the oxygen in the gum metal chemical composition could help retard the  $\alpha''$ -phase transformation [16,30], we intended to eliminate the possibility of forming  $\alpha''$ -phase by using a moderate cooling rate.

## 2.2. Experimental details

Gum metal with a composition of Ti-35.7Nb-1.9Ta-2.8Zr-0.40 (wt.%) was produced via arc-melting under argon atmosphere and cast into a rectangular copper mold. The ingot was subsequently annealed for 4 h at 1200 °C for homogenization and then furnace cooled. The average initial grain size ( $d$ ) of the as-solution treated (ST) material was ~60  $\mu$ m. The rectangular block was cold rolled at RT to ~80% thickness reduction to obtain the described starting material.

All heat treatments were carried out on rectangular samples (6 × 4 × 1 mm<sup>3</sup>) in a DIL805A/D dilatometer (Bähr Thermoanalyse GmbH), which enables an accurate control of temperature, heating/cooling rate, and atmosphere. Argon and helium were used respectively as the protecting atmosphere during holding and as the cooling agent. A newly upgraded multi-probe microstructure tracking method [31] was used to study the primary recrystallization behavior. Among the partially recrystallized states, the 20% (800°C-60 s) and 70% (800°C-300 s) recrystallized materials were selected for mechanical property investigations. Some partially recrystallized materials were additionally aged at 350 °C for 2 h to study the  $\omega$ -phase distribution.

All samples probed by scanning electron microscope (SEM) were wet-ground and polished. Final polishing was carried out using a solution of silica particle suspension with 25% H<sub>2</sub>O<sub>2</sub>. The microstructures in all states were characterized in a Zeiss-Crossbeam XB 1540 FIB-SEM (Carl Zeiss SMT AG). A EDAX/TSL system (AMETEK GmbH) equipped with a Hikari camera was used for electron backscatter diffraction (EBSD) measurements. Secondary electron (SE) and backscattered electron (BSE) imaging were conducted using an accelerating voltage of 15 or 30 kV. The recrystallization fraction ( $f_{\text{Rex}}$ ) was estimated using two methods: (i) large field (~200 × 500  $\mu$ m<sup>2</sup> in each state) EBSD grain average misorientation maps to differentiate the recrystallized and recovered<sup>3</sup> zones; (ii) color orientation contrast images of an integrated area of ~1 × 1.5 mm<sup>2</sup> in each state, taken in a Zeiss Merlin equipped with a Bruker EBSD system (Bruker Nano GmbH), to yield adequate

statistics. Color orientation contrast images, captured and integrated by three forward-mounted backscatter detectors positioned below the EBSD detector, assign different colors to pixels with respect to their orientation, as the electron beam is raster scanned across the specimen surface [32].

Transmission electron microscopy (TEM) specimens were lifted out following a site-specific method [33] in a dual-beam focused ion beam (FIB) Helios Nanolab 600i (FEI). TEM observations were performed in a JEOL JEM-2200 FS (JEOL GmbH) at an operating voltage of 200 kV, through which bright field (BF), dark field (DF) images and selected area diffraction patterns (SADP) were recorded by a Gatan CCD camera (Gatan, Inc.). Scanning transmission electron microscopy (STEM) images were captured using a scanning transmission electron imaging (STEI)-BF detector with a 100 cm camera length.

Dog-bone-shaped tensile samples (gauge geometry: 4 × 2 × 1 mm<sup>3</sup>) were cut by electrical discharge machining (EDM) with the gauge length parallel to the rolling direction (RD). Tensile tests were carried out using a 5 kN Kammrath & Weiss tensile stage coupled with in-situ imaging of speckled patterns on tensile sample surfaces using a high speed camera. The data were used for digital image correlation (macro-DIC: spatial resolution ≈ 120  $\mu$ m) analyses performed by employing the ARAMIS software (GOM GmbH). To study the deformation mechanisms, in-situ tensile tests were conducted using a SEM tensile stage designed in house, applying a recently developed correlative microstructure and DIC micro-strain mapping method [34]. In each deformation stage, micro-strain was mapped with 0.25  $\mu$ m spatial resolution, and the microstructure was imaged by BSE (also by EBSD in selected stages). Note that due to the difference of the spatial resolutions between the macro- and micro-DIC strain measurements, percentage and rational numbers are used here respectively for clarity.

The heights of the deformation-induced slip steps that appeared on the pre-polished tensile sample surfaces were measured with a NI/Veeco dimension 3100 atomic force microscope (AFM) operated in tapping mode. The lateral resolution of a scan map was set as 512 points along a distance of 30  $\mu$ m. A scan rate of 0.25 Hz and a tip velocity of 25  $\mu$ m s<sup>-1</sup> were used for the measurements. The data analysis was performed with the help of the Gwyddion software following a three-point plane correction of the zero level. The heights extracted as line profiles were averaged within a 1  $\mu$ m width along the drawn line.

Nanoindentation tests were carried out using a Hysitron Tribo-Scope 950 nanoindentation system with a Berkovich shaped indenter in a load-controlled mode and with a maximum load of 2500  $\mu$ N. The hardness of a matrix of 10 × 10 indents with a spacing of 15  $\mu$ m were mapped.

## 3. Results

### 3.1. Recrystallization kinetics and microstructure evolution

Recrystallization kinetics curves at 800 °C (Fig. 1a) obtained from EBSD maps (solid line) and color orientation contrast images (dashed line) reveal consistent trends that follow the general recrystallization kinetics curve of single phase materials [7]. 20% and 70% recrystallized materials were selected for further characterization, since they show representative microstructures of the nucleation stage and of the grain impingement stage. In all microstructures shown in Fig. 1, the top and bottom parts of the EBSD maps are taken from the center layer and the roll contact surface, respectively.<sup>4</sup> The image quality (IQ) overlaid inverse pole figure

<sup>2</sup> This is following the assumption that recovery generally has a lower activation energy than recrystallization at high temperatures [7].

<sup>3</sup> Recovered describes a microstructure state that is in recovery.

<sup>4</sup> In the roller contact surface, ~100  $\mu$ m thick zone was excluded due to low EBSD indexing (confidence index < 0.1).

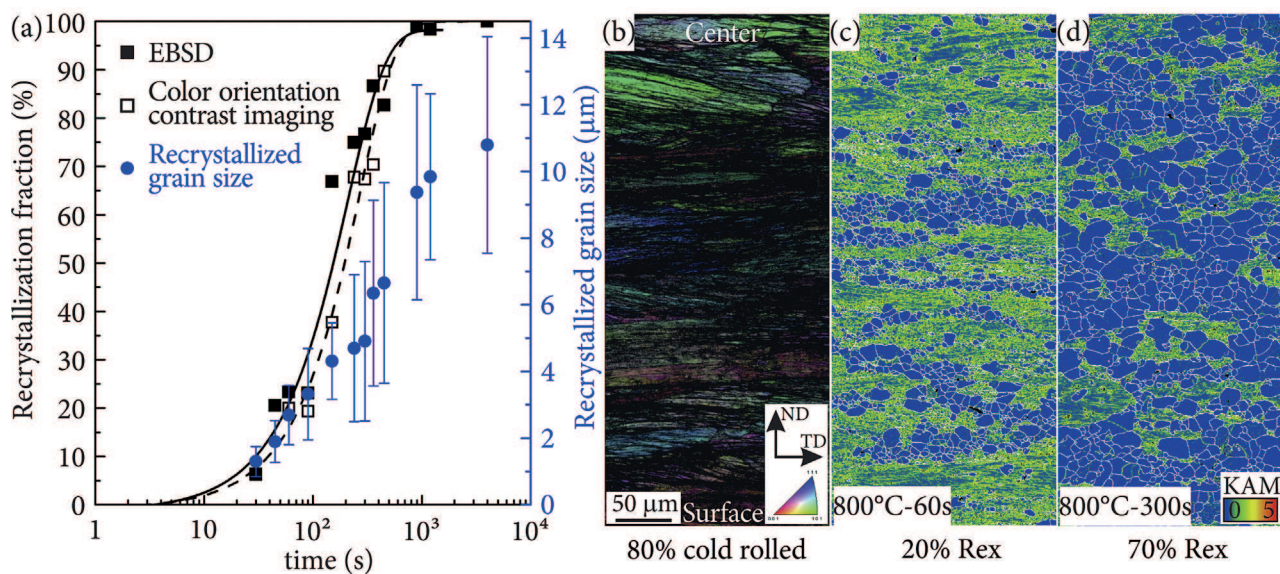


**Fig. 1.** Recrystallization kinetics curves and microstructure evolution during recrystallization of gum metal at 800 °C. **(a)** Recrystallization kinetics curves and recrystallized grain size evolution with error bars showing the standard deviation. The recrystallization kinetics curves were obtained from both EBSD and color orientation contrast images, which assign different colors to pixels with respect to their orientation during raster scanning of the electron beam. The half cross-section microstructures of the **(b)** 80% cold rolled, **(c)** 20% and **(d)** 70% recrystallized materials are shown as EBSD IQ overlaid IPF map and KAM maps with white HAGBs. Recrystallized grains are identified as the grains with low KAM and surrounded by HAGBs. Rex: recrystallized; ND: normal direction; TD: transverse direction; IQ: image quality; IPF: inverse pole figure; KAM: kernel average misorientation; HAGB: high angle grain boundary. (For interpretation of the references to colour in this figure legend, the reader is referred to the web version of this article.)

(IPF) map of the 80% cold rolled material (Fig. 1b) shows elongated prior deformed grains with an increasing density of shear bands from the center to the surface. The kernel average misorientation (KAM) map of the 20% recrystallized microstructure (Fig. 1c) shows that most of the recrystallized grains form chains that align in the RD and that some individual grains sit in the center layer. On the other hand, in the 70% recrystallized material (Fig. 1d) recovered islands are surrounded by larger recrystallized grains as compared to those in the 20% recrystallized state.

To understand the microstructure evolution during partial recrystallization, a recently developed microstructure tracking methodology was employed [31]. It is intrinsically challenging to study the recrystallization behavior by 2D observations owing to the unknown 3D morphology of the recrystallized grains. However, careful inspection of the 2D microstructure can still provide detailed information (Fig. 2). Fig. 2a, c and Fig. 2b, d shows respectively the IQ overlaid IPF and KAM maps of a selected area in the center layer of a cold rolled specimen before and after 20% recrystallization treatment (800 °C–60 s). By identifying the recrystallized grains (Fig. 2b and d) and labeling their relative positions with arrows (Fig. 2a and c), three types of recrystallization locations are recognized: shear bands (yellow arrows), high angle grain boundaries (HAGBs) of the prior grains (white arrows) and pre-existing NbO inclusions (red arrows). The recrystallized grains first appear in the vicinity of the HAGBs and shear bands, which is consistent with the commonly reported recrystallization behavior of single phase materials [7]. These recrystallized grains are either nucleated from those regions or grown from the prior subgrains in the vicinity to minimize the stored deformation energy. This explains the formation of chains of recrystallized grains aligned in the RD in the 20% recrystallized material (Fig. 1c). Those individual recrystallized grains (red arrows) are formed through particle stimulated nucleation (PSN) [7] around the NbO inclusions.

The orientation distribution functions (ODFs) of this specific area (Fig. 2) before and after recrystallization are plotted in Fig. 2e, with important texture components schematically overlaid on the ODF of the 80% cold rolled state. The comparison between the two

ODFs reveals that the  $\alpha_{\text{bcc}}$ -fiber intensity (green arrow) decreases and the  $\gamma_{\text{bcc}}$ -fiber intensity (blue arrows) increases during recrystallization, which agrees with the general evolution of the bcc texture during recrystallization [35,36].

Neither  $\alpha$ -phase nor martensitic  $\alpha''$ -phase was observed in either the 20% or the 70% recrystallized microstructure. Athermal  $\omega$ -phase is expected in the partially recrystallized microstructure; thus, its presence was carefully investigated by TEM. Fig. 3a and d shows STEM images of the areas containing recrystallized grains and recovered zones, in which the average misorientations between a pair of adjacent subgrains and a subgrain with its neighboring recrystallized grain are shown and indicated by yellow arrows. The  $[110]_{\beta}$  SADPs were captured from both the recovered subgrain (Fig. 3b) and the recrystallized grain (inset of Fig. 3e) using exactly the same imaging conditions<sup>5</sup> for TEM. Both SADPs show profuse diffuse streaks along the  $q_{211}$ -type reciprocal vectors. These features are generally regarded as an indication of the incommensurate athermal  $\omega$ -phase with partially collapsed  $\{222\}_{\beta}$  planes observed also in undercooled or irradiated materials [15,37]. However, this point is still debated due to the difficulty in imaging the  $\omega$ -phase with such weak reflections [15,17,30,38]. In this work, these diffuse streaks are interpreted to show the presence of  $\omega$ -phase, based on former works on gum metal of this composition [14,18,26]. In addition, extra efforts were placed on imaging the  $\sim 1.95$  nm diameter  $\omega$ -precipitates in the recrystallized grain using long exposure DF images (Fig. 3e). However, it was not possible to capture a clear DF image from the recovered subgrains. To compare the volume fractions of the athermal  $\omega$ -phase in these two zones, intensity profiles of the diffuse streaks along the four  $q_{211}$ -type reciprocal vectors (green lines in Fig. 3b and blue lines in the inset of Fig. 3e) were captured, averaged, and plotted in Fig. 3c. The higher  $\omega$ -phase reflection intensities from the recrystallized grains

<sup>5</sup> The imaging conditions (e.g. spot size, exposure time) were kept constant to ensure that the intensities of the reflections in the SADPs were determined by the relative volume fractions of the constituent phases.



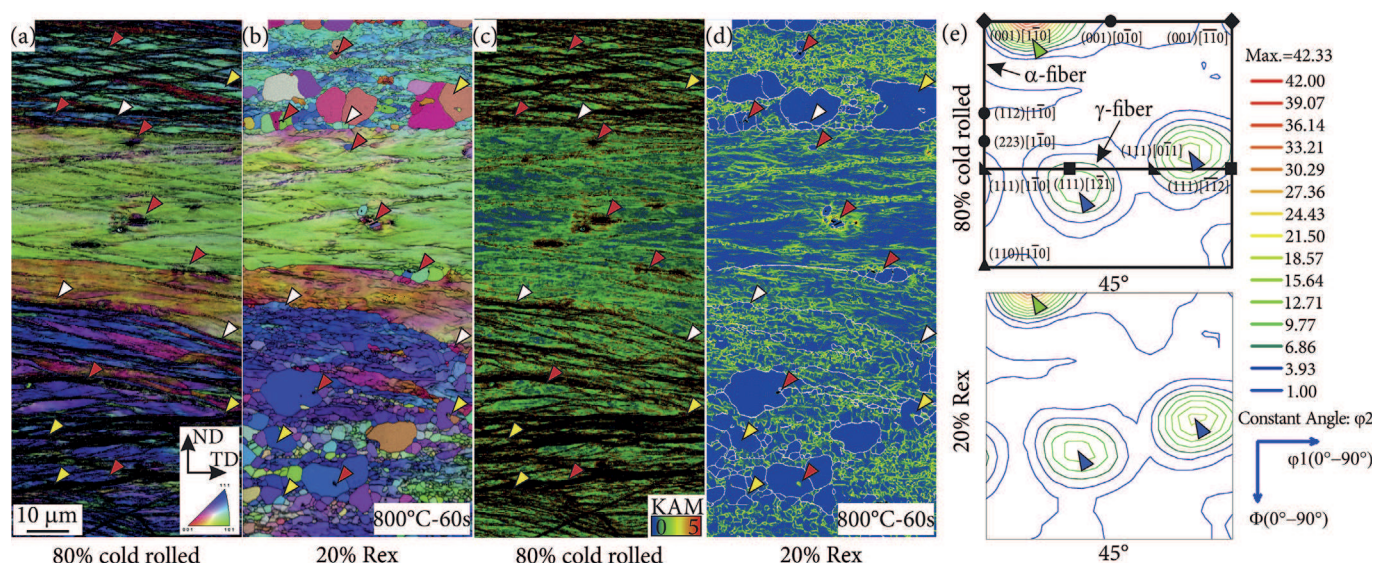


**Fig. 2.** Quasi-in-situ tracking of the microstructure evolution of a selected area before and after 20% recrystallization treatment. EBSD IQ overlaid IPF and KAM maps show respectively the microstructures of (a and c) the 80% cold rolled and (b and d) the 20% recrystallized materials. The recrystallization locations at the shear bands, HAGBs of prior grains (the grains before cold rolling) and pre-existing NbO inclusions are indicated with yellow, white and red arrows, respectively. The evolution of the micro-texture before and after recrystallization is shown as ODF in (e). ODF: orientation distribution function. (For interpretation of the references to colour in this figure legend, the reader is referred to the web version of this article.)

than from the recovered zones provides the first indication that the former has a higher volume fraction of the athermal  $\omega$ .

Isothermal  $\omega$  is commonly recognized as grown from the prior athermal  $\omega$  [37], therefore, an aging treatment was carried out at 350 °C for 2 h to obtain large isothermal  $\omega$  to validate the observation on the athermal  $\omega$  (Fig. 3c). The isothermal  $\omega$ -precipitates are generally shown in lenticular shape in the DF images (Fig. 3g and i). The comparison between the superimposed images of the  $\omega$ -phase, which were extracted from the DF images with the same threshold settings, reveals a higher volume fraction of the  $\omega$ -phase in the recrystallized grain (~13 vol %, Fig. 3j) than that in the recovered subgrain (~7 vol %, Fig. 3h). Furthermore, the intensity profiles averaged from the four  $q_{211}$ -type reciprocal vectors, marked in the inset SADPs in Fig. 3g and i, also show much higher intensities of the  $\omega$ -phase reflections from the recrystallized grain (Fig. 3f). This is yet another indication that the recrystallized grains contain a higher volume fraction of the  $\omega$ -phase than the recovered subgrains. In summary, Fig. 3 demonstrates that the moderate cooling rate of  $-50 \text{ K s}^{-1}$  successfully prevented the formation of both  $\alpha$ - and  $\alpha'$ -phase and enriched nano-sized  $\omega$ -phase in the recrystallized grains.

### 3.2. Mechanical properties and deformation mechanisms

In Fig. 4a, the engineering stress-strain curves show that the ultimate tensile strength (UTS) and the total elongation (TE) of the 20% recrystallized material increase by ~40% and ~70% compared to the as-ST and the 80% cold rolled states, respectively. These mechanical properties are compared to those of other  $\beta$ -Ti alloys with similar gauge geometries [12,19,39–43] to the samples used in this work in Fig. 4b. The caption provides a more detailed description of the data points. Typically, mechanisms or processing methods that increase the strength decrease the ductility and vice versa, a phenomenon referred to as the inverse strength-ductility relationship. This was observed for different factors in the literature [19,39–43], which is represented by the datasets marked with grey dotted lines in Fig. 4b. However, the partially recrystallized gum metals exhibit mechanical properties (pink and purple circles) that exceed the

inverse strength-ductility relationship established by current Ti-Nb-based alloys.

To identify the relative hardness of the recovered and recrystallized zones, nanoindentation tests were conducted. The indentation size effect [44] and the grain boundary vicinity effect set the lower and the upper limits for the size of the applied indents. As a result, a maximum load of 2500  $\mu\text{N}$  was used considering an average recrystallized grain size of ~2.1  $\mu\text{m}$  and a ratio of 2.5 between the plastic deformation zone and the contact diameter of an indent [45]. By identifying the indents in the recrystallized grains and the recovered zones, the average nano-hardness values of these two constituents were calculated and plotted in Fig. 5. It is shown that the recrystallized grains have a slightly higher hardness than the recovered zones. This phenomenon is discussed in section 4.1 with respect to their specific hardening mechanisms, namely, grain refinement with the associated Hall-Petch effect,  $\omega$ -precipitate hardening in the recrystallized grains, and deformation hardening via subgrains in the recovered zones.

To uncover the deformation micro-mechanisms, in-situ SEM tensile tests coupled with DIC micro-strain mapping [34] were conducted on the 20% recrystallized samples. The von Mises equivalent strain is used for the micro-strain mapping because of its positive correlation to the statistically stored dislocation (SSD) density. Fig. 6a<sub>1</sub> and a<sub>2</sub> show the BSE image and the strain map of an undeformed microstructure. When the average von Mises strain over the studied area ( $\varepsilon$ ) is ~0.01 (Fig. 6b<sub>2</sub>), i.e. in the elastic regime, the strain is uniformly distributed with no deformation features, except for some changes in the BSE contrast due to local lattice rotation (red arrows). Plastic deformation is initiated ( $\varepsilon \approx 0.02$ , Fig. 6c<sub>1</sub>) at a high yield strength (1130 MPa), when a few dislocation slip lines appear in the recovered zones and strain localization is captured in the recovered zones (grey arrows in Fig. 6c<sub>2</sub>) and at the HAGBs and triple junctions of the recrystallized grains (white arrows in Fig. 6c<sub>2</sub>). These dislocations can glide over large distances since they can penetrate the low angle grain boundaries (LAGBs) that surround the subgrains. At a strain level  $\varepsilon \approx 0.03$ , the plastic deformation proceeds through activation of the same slip system(s) (Fig. 6d<sub>1</sub>). Furthermore, the BSE contrast between adjacent



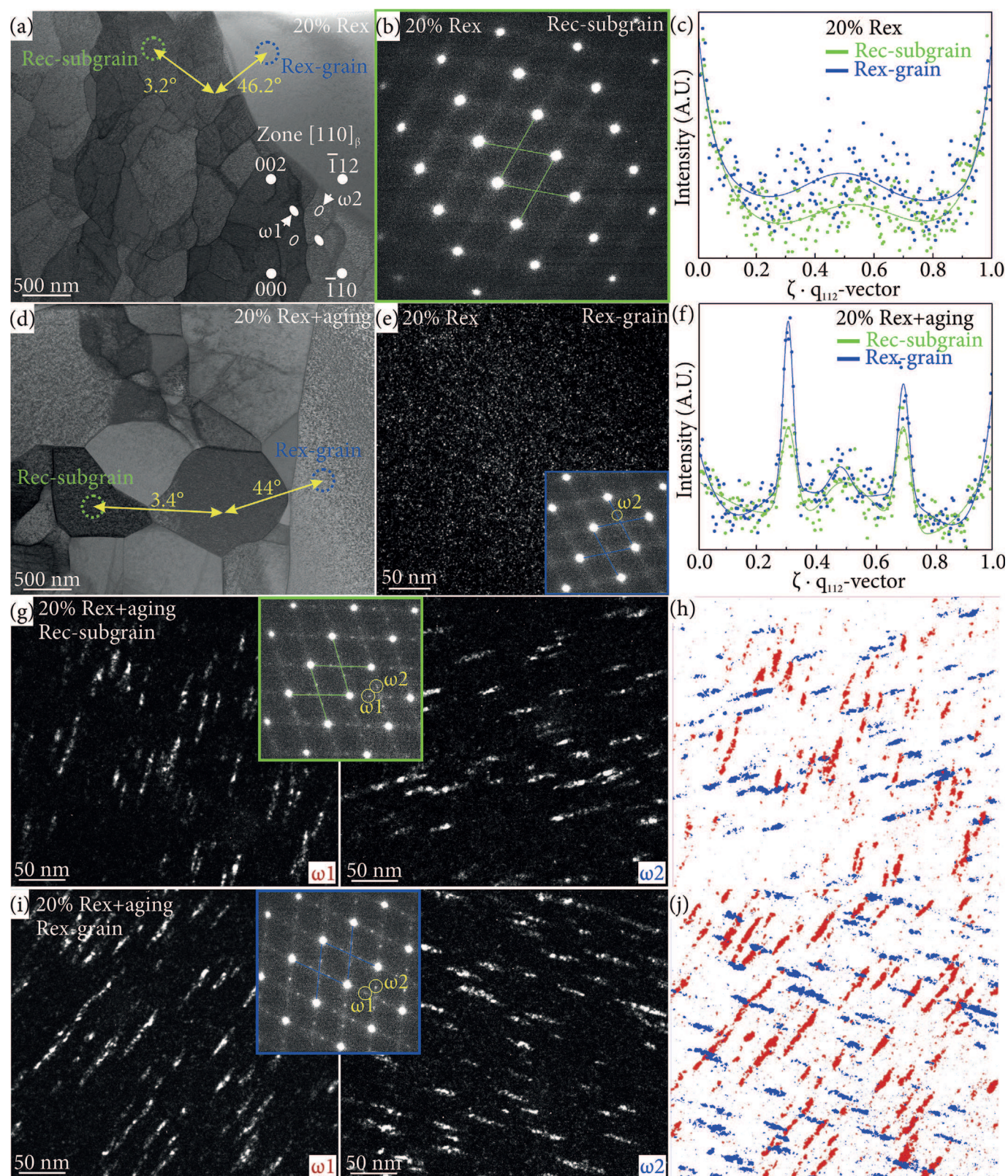


**Fig. 3.** Distribution of nano-sized  $\omega$ -phase after recrystallization. STEM images of the (a) 20% recrystallized and (d) 20% recrystallized and aged (350°C-2 h) materials. The areas in the recovered subgrains and the recrystallized grains, from which the SADPs and the DF images are captured, are marked by the green and blue dashed circles, respectively. The average misorientations between a pair of adjacent subgrains and a subgrain with its neighboring recrystallized grain are also shown and indicated with yellow arrows. The key diagram of the SADP with the  $[110]_\beta$  zone axis is shown as inset in (a). (b) and (e) show, respectively, the SADP of the recovered subgrain and DF image of the athermal  $\omega$ -phase with the SADP as inset, captured from the area shown in (a). Intensity profiles averaged from the four green lines in (b) and the blue lines in the inset of (e) for the 20% recrystallized material, and in the insets of (g) and (i) for the 20% recrystallized and aged material are plotted in (c) and (f). The DF images of  $\omega$ -phase in the aged material with two different variants are captured from both (g) the recovered subgrain and (i) recrystallized grain. (h) and (j) show the superimposed images extracted with the same threshold settings from (g) and (i). Rex: recrystallized; Rec: recovered. (For interpretation of the references to colour in this figure legend, the reader is referred to the web version of this article.)



subgrains progressively changes, whereas the recrystallized grains show no plastic strain accumulation except for the largest grain (Fig. 6c<sub>2</sub> and d<sub>2</sub>).

As deformation proceeds, another type of dislocation slip lines, which create more pronounced surface steps and in turn stronger SE contrast than the slip lines in the recovered zones (Fig. 6), appears in the recrystallized grains. Following this observation, these two types of dislocation slip lines were studied using post-mortem AFM at the macro-DIC local strain levels ( $\epsilon'$ ) of ~5% and ~15% (Fig. 7). Note that  $\epsilon'$  is the true strain of a much larger area than the area studied by micro-DIC in Fig. 6, due to the much lower spatial resolution of macro-DIC (120  $\mu\text{m}$ ) as compared to micro-DIC (0.25  $\mu\text{m}$ ). Fig. 7c and f shows that the heights of the surface steps along the blue arrows (blue curves) in the recrystallized grains are generally <5 nm, whereas those in the recovered zones (red curves) are a factor 2–4 higher (10–20 nm). The slip lines across the black arrows (black curves) show two characteristics: (i) they have large step heights ( $\epsilon' \approx 5\%$ : 13–35 nm and  $\epsilon' \approx 15\%$ : 19–72 nm); (ii) they are parallel to the  $\{112\}_\beta$  plane traces, which indicates their formation by dislocation activity on the  $\{112\}_\beta$  planes. The number of dislocations that moved out of the pre-polished surface on a specific slip plane can be estimated from the height of the surface step and the Burgers vector of the dislocation. As the Burgers vector of the  $a/2\langle 111 \rangle$ -type dislocation in gum metal is ~0.286 nm [26], the slip step (yellow arrows in Fig. 7) with a height of 34.4 nm is formed by the slip of ~120 dislocations. This phenomenon, that a large number of dislocations slip on a single  $\{112\}_\beta$  slip plane, is consistent with the  $\omega$ -phase induced dislocation channeling reported as a deformation mechanism in gum metal [26].

When the engineering strain ( $\epsilon_{\text{Eng}}$ ) reaches 13%, the plastic strain localizes in the diffuse necking region, where the micro-strain ( $\epsilon$ ) is mapped in the same way as in Fig. 6. The position of a selected area on the tensile sample right before fracture is shown by a black rectangle in Fig. 8a. When  $\epsilon \approx 0.13$  (Fig. 8b<sub>1</sub> and b<sub>2</sub>), the plastic deformation of the recovered zones is generally carried by two dislocation slip systems, whereas the three recrystallized grains (marked as A, B and C) show distinctly different behavior: dislocation channeling lines (yellow arrows) appear exclusively in grain A, but together with the conventional dislocation slip lines in grain B; grain C deforms only by conventional dislocation slip. Upon further straining ( $\epsilon \approx 0.18$  in Fig. 8c<sub>1</sub> and c<sub>2</sub>), no obvious change is observed except that more dislocation channeling lines appear in grain B. To study the mechanical behavior of the microstructure further, the strain increments (from  $\epsilon \approx 0.13$  to  $\epsilon \approx 0.18$ ) averaged respectively over the pink-red lines and over the green-olive lines in the strain map (Fig. 8c<sub>2</sub>) are plotted in Fig. 8d. Since the left side of the GB in the selected area is closer to the fractured surface (black dashed line in Fig. 8a), the strain increments here (pink and green) are expected to be much higher than that on the right side (red and olive). However, both strain increment profiles in Fig. 8d show, surprisingly, higher strain increments on the right-hand side of the GB than that on the left-hand side. This result indicates that the strain might partition from the recovered zones to the recrystallized grains as the plastic deformation localizes.

## 4. Discussion

### 4.1. Strength of the recovered zones and recrystallized grains

We first discuss the relative contributions of the recovered and recrystallized zones to the improved yield strength of the 20% recrystallized gum metal.

The recovered zones are hardened by the residual pre-deformation stored in the form of subgrains. As the subgrains are

formed by dislocation entanglement and annihilation during recovery, we expect the amount of the residual SSDs to be small, i.e. causing a negligible effect on the yield strength. Considering the subgrain boundaries ( $<15^\circ$ ) as a collection of geometrically necessary dislocations (GNDs) to accommodate the misorientation [28, 58], their effect on the yield strength can be estimated by the empirical law [46,47]:

$$\Delta\tau = GKb/D \quad (1)$$

By using the shear modulus  $G \approx 25$  GPa, Burgers vector  $b \approx 0.286$  nm, subgrain size  $D \approx 550$  nm, and the constant  $K \approx 10$  [46,47] for gum metal,  $\Delta\tau$  was calculated to be ~130 MPa. Following this,  $\Delta\sigma \approx 319$  MPa was obtained from  $\Delta\tau$  considering a Schmid factor  $m$  of 0.408, as most of the crystal lattices in the recovered zones pertain to the  $\alpha_{\text{bcc}}$ -fiber texture, i.e.  $\langle 110 \rangle$ //tensile axis (TA). When assuming that  $\Delta\sigma$  is the increase of the yield strength due to the presence of subgrain boundaries compared to the as-ST gum metal, the yield strength of the recovered zones is calculated to be ~1124 MPa.

The recrystallized grains are strengthened by their refined grain size and nano-sized  $\omega$ -precipitates. When considering the RD-aligned chains of the recrystallized grains as a contiguous constituent along the TA, the yield strength of the recrystallized grains can be estimated by extrapolating the Hall-Petch plot [48,49] of gum metal, based on:

$$\sigma_y = \sigma_0 + kd^{-1/2} \quad (2)$$

where  $\sigma_0$  is the yield strength of a single crystal in the limit of a large grain size  $d$ , and  $k$  is the Hall-Petch constant [6]. To obtain the Hall-Petch plot, tensile test data of gum metals were collected from former works of the authors and plotted with respect to  $d^{-1/2}$  in Fig. 9. Note that this Hall-Petch plot includes the  $\omega$ -precipitation hardening effect by assuming that these gum metals contain  $\omega$ -phase of the same size and volume fraction. By extrapolating the Hall-Petch plot, the yield strength of the recrystallized grains was calculated to be 1593 MPa (pink square).

These simple considerations indicate that the strengthening effects of grain refinement and precipitation in the recrystallized grains are more effective than that of the subgrains in the recovered zones. More importantly, in agreement with the nanoindentation results, it is validated that the recrystallized grains (1593 MPa) contribute more to the yield strength of the 20% recrystallized gum metal (1130 MPa) than the recovered zones (1124 MPa).

### 4.2. Deformation mechanisms to improve the ductility

One of the most effective ways to improve the ductility of metallic materials is to consume the work hardening capabilities conservatively by sequentially activating the same or different deformation mechanisms in different microstructural constituents. This is achieved in this work by the sequential activation of conventional dislocation slip and dislocation channeling.

Dislocation channeling is a massive localized dislocation activity due to the constraint of dispersedly distributed nano- $\omega$ -precipitates in gum metal [26]. To act as effective dislocation barriers,  $\omega$ -precipitates with sufficiently large size and volume fraction (such as the ones in the recrystallized grains, Fig. 3), are required for the activation of dislocation channeling. The  $\omega$ -phase transformation can be strongly retarded by increasing the stability of the  $\beta$ -phase, i.e. by increasing the content of  $\beta$ -phase stabilizers, e.g. Nb and Ta in gum metal [50,51]. In addition, oxygen and Zr are also known as effective additions to  $\beta$ -Ti alloy compositions against  $\omega$ -phase transformation [52–54]. Therefore, we consider it plausible

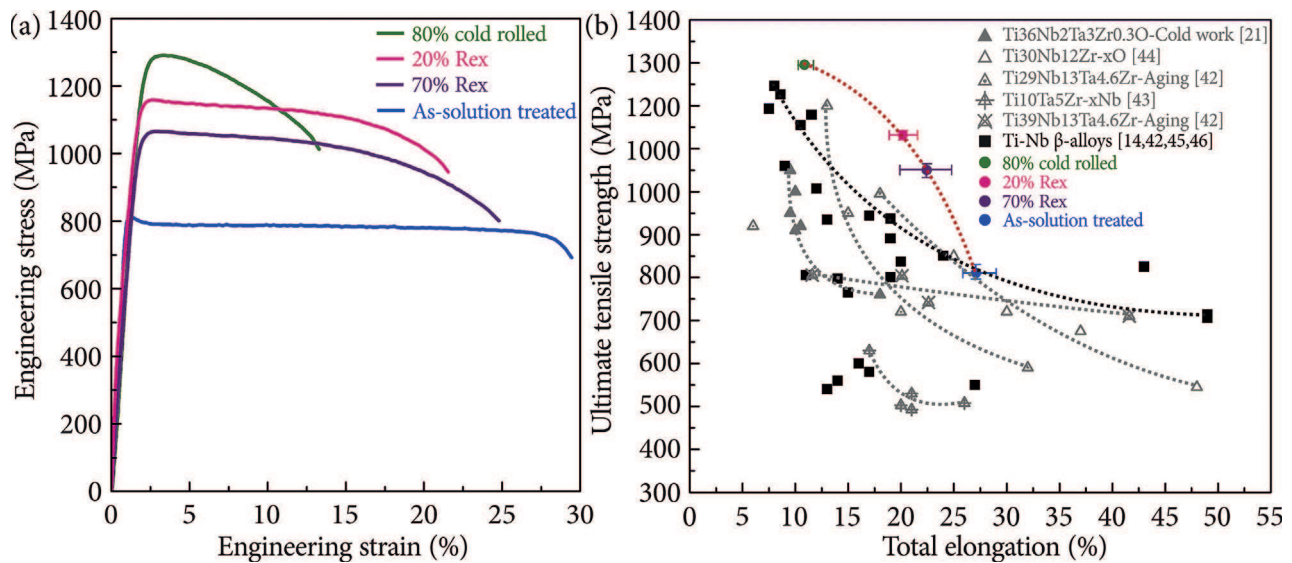


**Fig. 4.** Mechanical properties of the studied materials. (a) Engineering stress-strain curves of the 80% cold rolled, 20% recrystallized, 70% recrystallized, and as-ST gum metal. (b) UTS vs. TE scatter plot of the mechanical properties of the studied materials in comparison to literature data. Data obtained in this work are plotted as circles with error bars showing the maximum and minimum scatter of the properties. Each set of grey triangles with the same inner symbol represents the influence of a single factor on the mechanical properties: e.g. filled grey triangles show the influence of the cold work on gum metal [19]; open grey triangles show the influence of oxygen content on Ti30Nb12Zr alloys [41]. Black rhombuses represent the data points extracted from different  $\beta$ -Ti alloys.

that the preferred elemental segregation to dislocations [6,7,55] increases the  $\beta$ -stability in the recovered zones. Thus, the recovered  $\beta$ -phase transforms to a lesser extent into the  $\omega$ -phase during cooling as compared to the recrystallized  $\beta$ -phase grains (Fig. 3). Moreover, interstitial oxygen is expected to exhibit the most

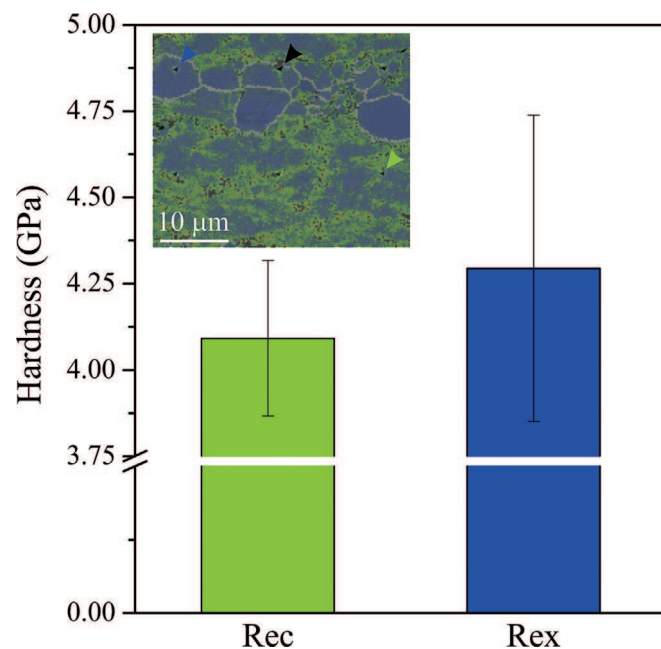


**Fig. 5.** Average nano-hardness of the recovered zones and the recrystallized grains in 20% recrystallized gum metal with the error bars showing the standard deviation. The inset shows the KAM map overlaid by a 30% transparent SE image of an example area with 6 indents. Blue and green arrows indicate the indents in the recrystallized and the recovered zones. Indents near grain boundaries and inclusions, such as the indent marked with the black arrow, were excluded from the analysis. KAM: kernel average misorientation; Rex: recrystallized; Rec: recovered. (For interpretation of the references to colour in this figure legend, the reader is referred to the web version of this article.)

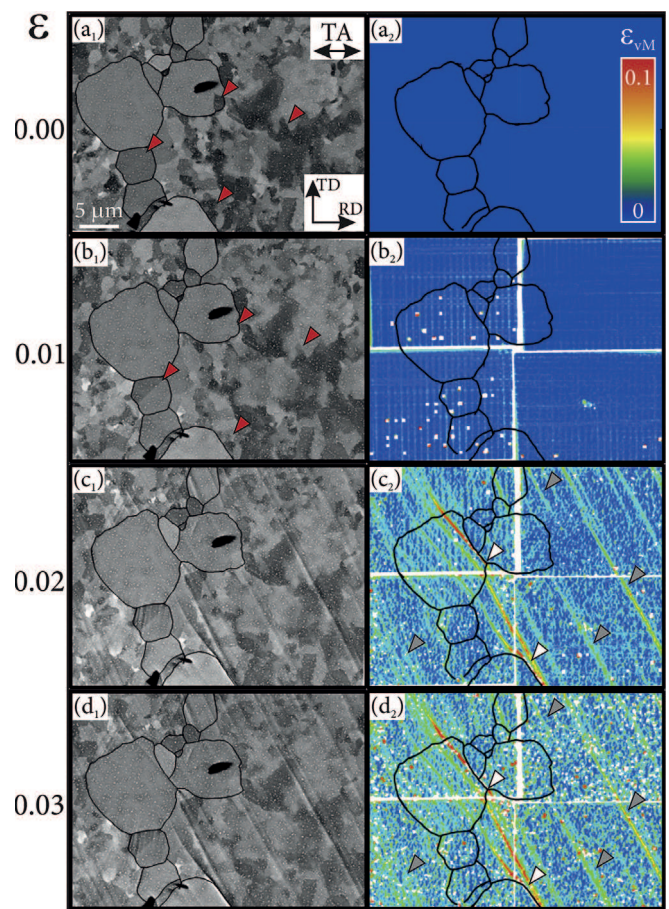


**Fig. 6.** Deformation mechanisms at the beginning of the plastic deformation of the 20% recrystallized material. (a<sub>1</sub>, b<sub>1</sub>, c<sub>1</sub>, d<sub>1</sub>) BSE images and (a<sub>2</sub>, b<sub>2</sub>, c<sub>2</sub>, d<sub>2</sub>) DIC micro-strain maps of a selected area at average von Mises strain (over the studied area) levels of 0, 0.01, 0.02 and 0.03. Black lines mark the HAGBs, and the two black particles are NbO inclusions. TA: tensile axis; BSE: backscattered electron; DIC: digital image correlation.



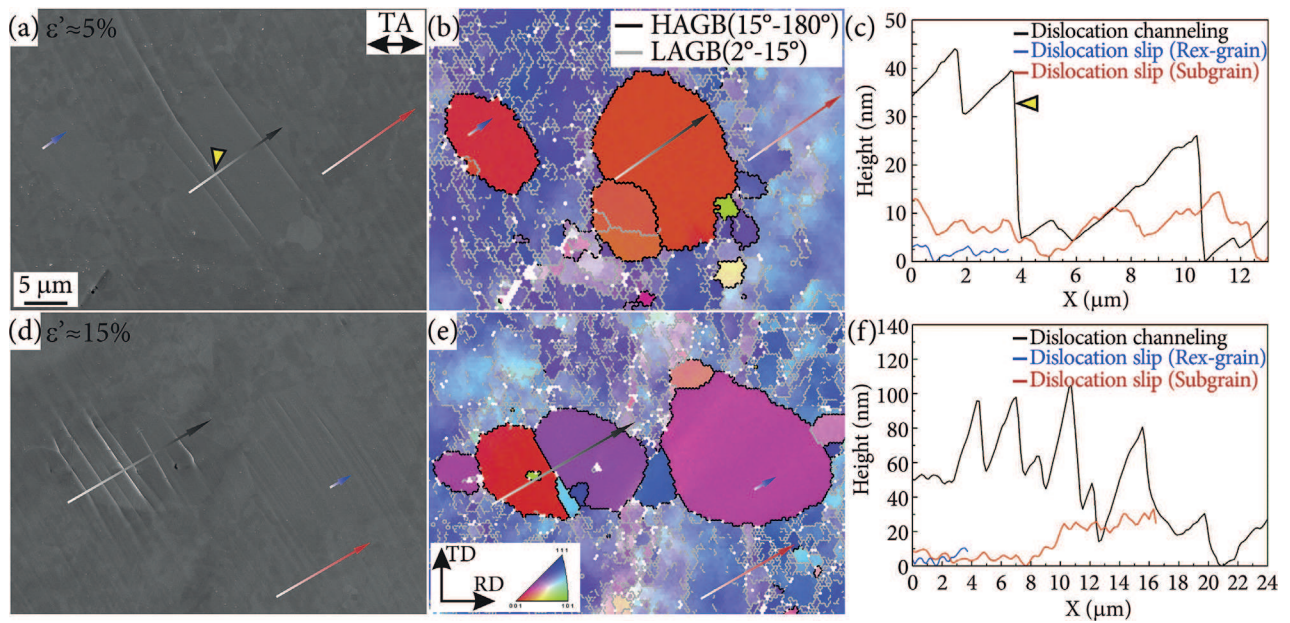


**Fig. 7.** AFM studies of the surface steps of conventional dislocation slip and dislocation channeling. (a, d) SE images and (b, e) IPF maps of two selected areas at  $\epsilon'$  of  $\sim 5\%$  and  $\sim 15\%$  (local strain calculated by macro-DIC). The height profiles of the surface steps obtained by AFM are plotted in (c) and (f) corresponding to the black, blue and red arrows shown in (a, b) and (d, e). Rex: recrystallized; AFM: atomic force microscopy; LAGB: low angle grain boundary. (For interpretation of the references to colour in this figure legend, the reader is referred to the web version of this article.)

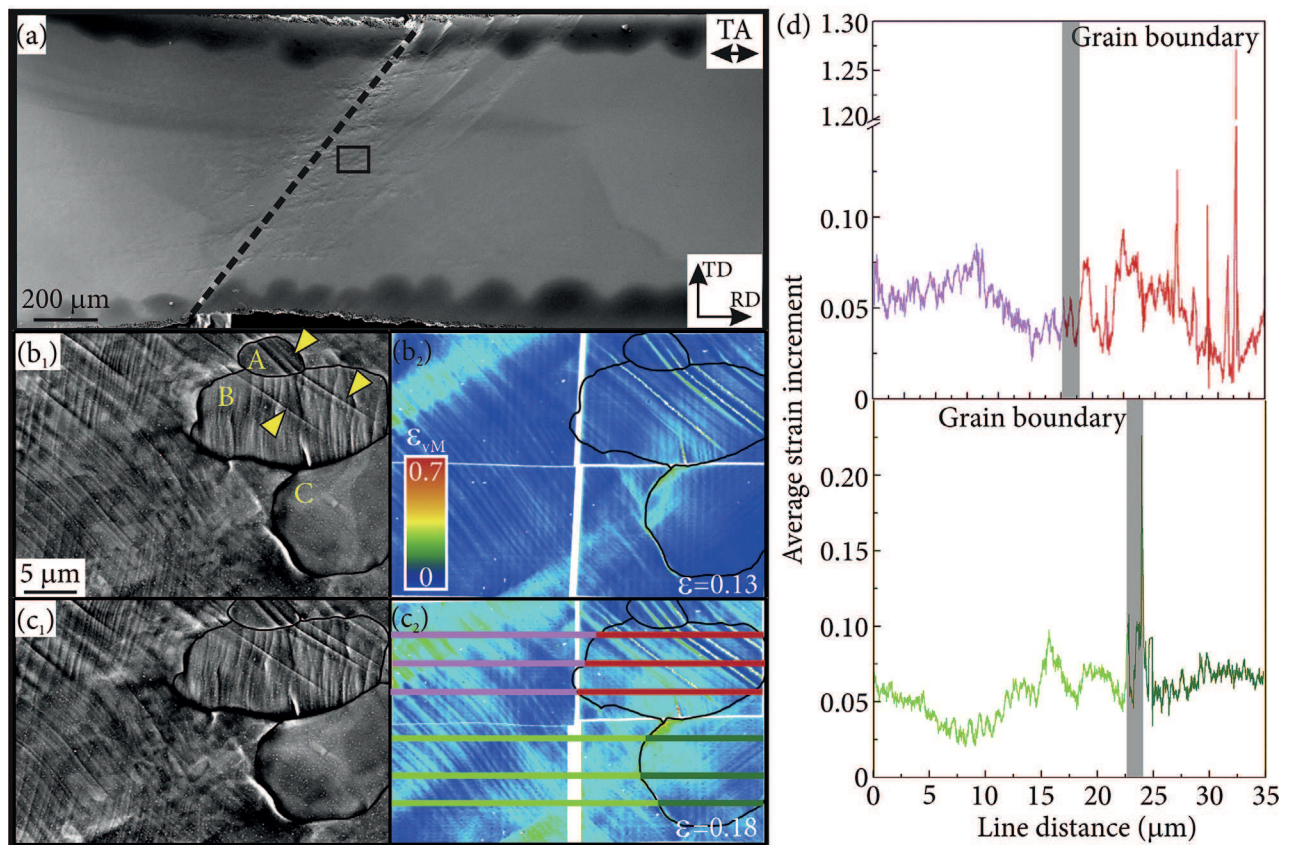


**Fig. 8.** Deformation mechanisms within the diffuse necking region of the 20% recrystallized sample. (a) SE image of the necking area of the in-situ SEM tensile sample just before fracture. (b<sub>1</sub>, c<sub>1</sub>) BSE images and (b<sub>2</sub>, c<sub>2</sub>) the micro-strain maps with black HAGBs of the area marked with the black rectangle in (a) at  $\epsilon \approx 0.13$  and  $\epsilon \approx 0.18$ . (d) The strain increment (from  $\epsilon \approx 0.13$  to  $\epsilon \approx 0.18$ ) profiles averaged over the pink-red lines and over the green-olive lines in the micro-strain map with the positions of the grain boundaries marked with a grey line. SE: secondary electron. (For interpretation of the references to colour in this figure legend, the reader is referred to the web version of this article.)



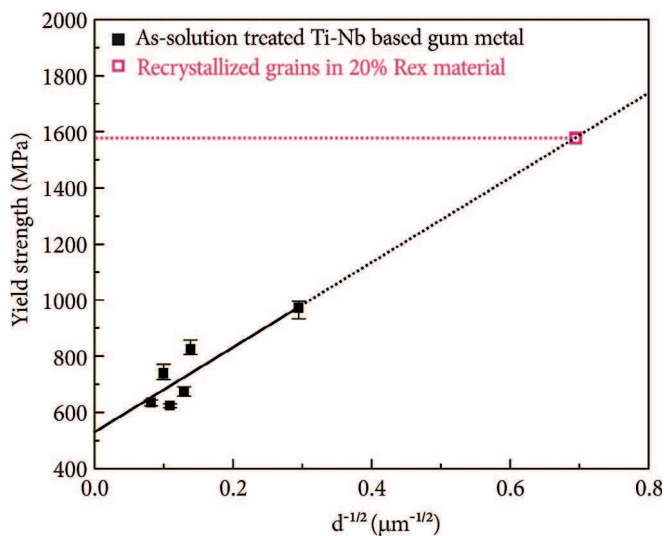


**Fig. 9.** Hall-Petch plot of yield strength vs.  $d^{-1/2}$  ( $d$ : average grain size, filled black squares) of gum metal, error bars showing the maximum and minimum scatter of the yield strength. Extrapolated data point for the 20% recrystallized grains are marked with the pink open square.  $\sigma_0 \approx 530.77$  MPa and  $k \approx 1503$  MPa  $\mu\text{m}^{-1/2}$  are obtained from the fitted equation of the Hall-Petch plot. (For interpretation of the references to colour in this figure legend, the reader is referred to the web version of this article.)

significant segregation trend compared to substitutional atoms such as Nb, Ta, and Zr, due to its small size and the short recrystallization annealing duration (60 s). This effect is not studied in this work (spatially-resolved oxygen mapping has several challenges) but is of interest for future studies.

Dislocation channeling in gum metal is activated due to partial dislocation slip on the  $\{112\}_\beta$  planes at an elevated critical resolved shear stress (CRSS). This leads to a local  $\omega$  to  $\beta$  back transformation and opens an  $\omega$ -free soft channel for subsequent dislocation slip [26]. Following this, many dislocations glide within the soft channel and form a pronounced surface step when they meet the pre-polished surface (Fig. 7). As the dislocation activity is constrained in a few softened channels, the interactions among dislocations on different slip planes are reduced. As a result, pronounced dislocation substructures such as cell blocks and dislocation cells do not

develop and thus also do not contribute to work hardening. In contrast, conventional dislocation slip is active in the  $\omega$ -lean recovered zones, where dislocations are more easily nucleated. This in turn results in a more homogeneous (less localized) dislocation activity that promotes the formation of distinct dislocation substructures. Therefore, dislocation channeling generally leads to high yield strength (due to  $\omega$ -precipitate hardening) and low work hardening, whereas conventional dislocation slip results in low yield strength and high work hardening. Due to their distinct mechanical response, dislocation channeling and conventional dislocation slip are activated in different deformation stages, which is discussed in the following.

Based on Figs. 6–8, the deformation sequence of the 20% recrystallized material can be divided into three stages as illustrated schematically in Fig. 10. In stage I, when the sample is first strained, the remaining glissile dislocations in the recovered zones, due to the low yield strength and insufficient constraint of  $\omega$ -precipitates, quickly activate and glide on their slip planes (Fig. 6). During this stage, only a few large recrystallized grains show dislocation activity; therefore, the plastic strain is mostly carried by the recovered zones (Fig. 6c<sub>2</sub> and d<sub>2</sub>). As the stress increases, the second or third slip systems initiate in the recovered zones and bring the deformation to stage II. During this stage, dislocation multiplication leads to continuous changes of the misorientation of the pre-existing LAGBs, which are revealed by the change of the crystallographic BSE contrast between adjacent subgrains. Along with the increasing stress, dislocation channeling also activates in a few recrystallized grains (Fig. 7a).

Stage III sets in when most of the strain hardening capacity of the recovered zones is exhausted, and the plastic strain localizes in the neck (tensile strain  $\approx 13\%$ ). In this stage, the strain partitions slightly to the recrystallized grains, where the strain hardening rate is more easily maintained by the  $\omega$ -precipitation hardening. This is observed in Fig. 8d, namely, that the strain increases more in the recrystallized grains, which are expected to have lower strain increments than the recovered zones due to the larger distance to the fracture surface. This dynamic strain partitioning effect has been previously reported to improve the mechanical properties of various materials, e.g. in TRIP-maraging steels [56,57], as plastic strain is carried by different microstructural constituents in different deformation stages. When the work hardening capacity of the recrystallized grains also approaches the limit, micro-voids

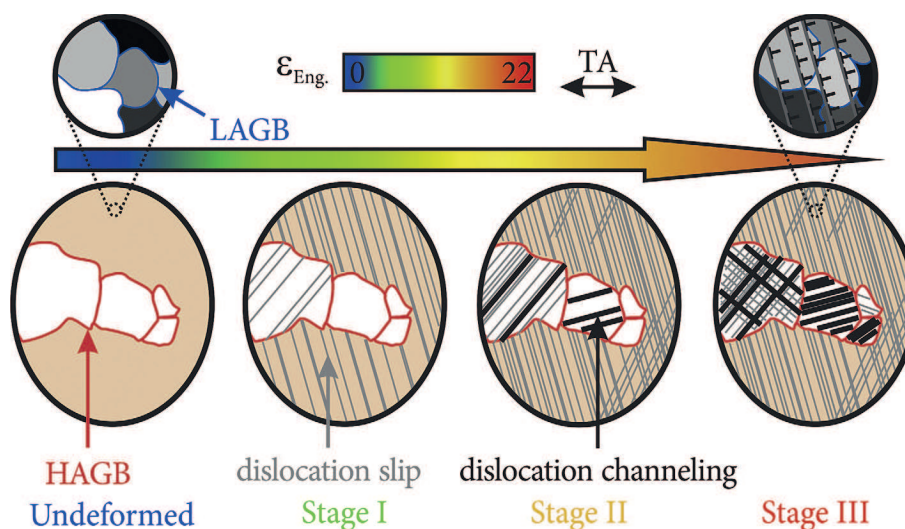


**Fig. 10.** Schematic sketch showing the deformation mechanisms of the 20% recrystallized material during tensile deformation. HAGB: high angle grain boundary; LAGB: low angle grain boundary.

form and coalesce until the material fracture with a TE of ~22%. This deformation sequence leads to the extended elongation of the partially recrystallized gum metal, which helps to achieve the enhanced strength-ductility combination.

## 5. Conclusions

We proposed a microstructure design approach which incorporates nano-precipitation in partial recrystallization. This approach was applied to a Ti-Nb based gum metal. The mechanical properties and deformation mechanisms of the achieved microstructure were investigated following a study of the recrystallization kinetics. The main conclusions are listed in the following:

1. The targeted microstructure is successfully achieved through partial recrystallization of the 80% cold rolled gum metal at 800 °C, followed by cooling with a moderate rate ( $-50 \text{ K s}^{-1}$ ). 20% recrystallization produces a microstructure, in which RD-aligned chains of ultrafine recrystallized grains ( $\sim 2.1 \mu\text{m}$ ) are embedded in the recovered subgrain-containing zones. The controlled cooling leads to enriched nano- $\omega$ -precipitates in recrystallized grains and depletion of  $\omega$  in the recovered zones, and hence the activation of dislocation channeling in the recrystallized grains.
2. The mechanical properties of both 20% and 70% recrystallized gum metal exceed the inverse strength-ductility relationship established by the literature data of metastable  $\beta$ -Ti alloys. However, the 20% recrystallized material with smaller recrystallized grains shows better mechanical properties ( $\text{UTS} \approx 1130 \text{ MPa}$ ,  $\text{TE} \approx 22\%$ ).
3. We attribute the improved strength-ductility combination to: (i) contributions from both the subgrain strengthening in the recovered zones and, to a greater extent, refined grains with nano- $\omega$  precipitation hardening in the recrystallized grains; (ii) conservative consumption of the work hardening capabilities via sequential activation of the conventional dislocation slip and dislocation channeling.

## Acknowledgements

The authors gratefully acknowledge financial support by the European Research Council under the EU's seventh Framework Program (FP7/2007-2013)/ERC grant agreement 290998 "Smart-Met". M.J. Lai expresses his gratitude to China Scholarship Council for the scholarship granted to support this work.

## References

- [1] Y.M. Wang, M.W. Chen, F.H. Zhou, E. Ma, High tensile ductility in a nano-structured metal, *Nature* 419 (2002) 912–915.
- [2] C.C. Koch, Optimization of strength and ductility in nanocrystalline and ultrafine grained metals, *Scr. Mater.* 49 (2003) 657–662.
- [3] F.X. Lin, Y.B. Zhang, N.R. Tao, W. Pantleon, D.J. Jensen, Effects of heterogeneity on recrystallization kinetics of nanocrystalline copper prepared by dynamic plastic deformation, *Acta Mater.* 72 (2014) 252–261.
- [4] S.A. Farzadfar, E. Martin, M. Sanjari, E. Essadiqi, M.A. Wells, S. Yue, On the deformation, recrystallization and texture of hot-rolled Mg–2.9Y and Mg–2.9Zn solid solution alloys—A comparative study, *Mater. Sci. Eng. A-Struct. Mater. Prop. Microstruct. Process* 534 (2012) 209–219.
- [5] N. Stanford, Micro-alloying Mg with Y, Ce, Gd and La for texture modification—a comparative study, *Mater. Sci. Eng. A-Struct. Mater. Prop. Microstruct. Process* 527 (2010) 2669–2677.
- [6] G. Gottstein, *Physical Foundations of Materials Science*, Springer, Heidelberg, Germany, 2004.
- [7] F.J. Humphreys, M. Hatherly, *Recrystallization and Related Annealing Phenomena*, Elsevier Ltd, Kidlington, Oxford OX5 1GB, UK, 2004.
- [8] P. Muneshwar, S.K. Aingh, K.N. Kumar, B. Pant, K. Sreekumar, Effect of cold working and heat treatment on recrystallization, mechanical properties and microstructure of high strength Ti15V3Al3Cr3Sn (Ti–beta) alloy, *Mater. Sci. Forum* 710 (2012) 521–526.
- [9] C.Y. Liu, B. Qu, Z.Y. Ma, M.Z. Ma, R.P. Liu, Recrystallization, precipitation, and resultant mechanical properties of rolled Al–Zn alloy after aging, *Mater. Sci. Eng. A-Struct. Mater. Prop. Microstruct. Process* 657 (2016) 284–290.
- [10] H.T. Wang, N.R. Tao, K. Lu, Strengthening an austenitic Fe–Mn steel using nanotwinned austenitic grains, *Acta Mater.* 60 (2012) 4027–4040.
- [11] O. Bouaziz, D. Barbier, P. Cugy, G. Petigand, Effect of process parameters on a metallurgical route providing nano-structured single phase steel with high work-hardening, *Adv. Eng. Mater.* 14 (2012) 49–51.
- [12] T. Saito, T. Furuta, J.H. Hwang, S. Kuramoto, K. Nishino, N. Suzuki, R. Chen, A. Yamada, K. Ito, Y. Seno, T. Nonaka, H. Ikehata, N. Nagasako, C. Iwamoto, Y. Ikuhara, T. Sakuma, Multifunctional alloys obtained via a dislocation-free plastic deformation mechanism, *Science* 300 (2003) 464–467.
- [13] W. Guo, M.Z. Qadir, S. Moricca, T. Eddows, M. Ferry, Microstructural evolution and final properties of a cold-swaged multifunctional Ti–Nb–Ta–Zr–O alloy produced by a powder metallurgy route, *Mater. Sci. Eng. A-Struct. Mater. Prop. Microstruct. Process* 575 (2013) 206–216.
- [14] J.-L. Zhang, C.C. Tasan, M.J. Lai, J. Zhang, D. Raabe, Damage resistance in gum metal through cold work-induced microstructural heterogeneity, *J. Mater. Sci.* 50 (2015) 5694–5708.
- [15] S. Banerjee, R. Tewari, G.K. Dey, Omega phase transformation – morphologies and mechanisms, *Int. J. Mater. Res.* 97 (2006) 963–977.
- [16] R.J. Talling, R.J. Dashwood, M. Jackson, D. Dye, On the mechanism of super-elasticity in Gum metal, *Acta Mater.* 57 (2009) 1188–1198.
- [17] T. Yano, Y. Murakami, D. Shindo, S. Kuramoto, Study of the nanostructure of Gum Metal using energy-filtered transmission electron microscopy, *Acta Mater.* 57 (2009) 628–633.
- [18] M.J. Lai, C.C. Tasan, J. Zhang, B. Grabowski, L.F. Huang, D. Raabe, Origin of shear induced  $\beta$  to  $\omega$  transition in Ti–Nb-based alloys, *Acta Mater.* 92 (2015) 55–63.
- [19] T. Furuta, S. Kuramoto, J. Hwang, K. Nishino, T. Saito, Elastic deformation behavior of multi-functional Ti–Nb–Ta–Zr–O alloys, *Mater. Trans.* 46 (2005) 3001–3007.
- [20] M. Geetha, A.K. Singh, R. Asokamani, A.K. Gogia, Ti based biomaterials, the ultimate choice for orthopaedic implants – a review, *Prog. Mater. Sci.* 54 (2009) 397–425.
- [21] K. Wang, The use of titanium for medical applications in the USA, *Mater. Sci. Eng. A-Struct. Mater. Prop. Microstruct. Process* 213 (1996) 134–137.
- [22] M. Niinomi, Mechanical biocompatibilities of titanium alloys for biomedical applications, *J. Mech. Behav. Bio. Mater.* 1 (2008) 30–42.
- [23] W.Y. Guo, H. Xing, J. Sun, X.L. Li, J.S. Wu, R. Chen, Evolution of microstructure and texture during recrystallization of the cold-swaged Ti–Nb–Ta–Zr–O alloy, *Metall. Mater. Trans. A-Phys. Metall. Mater. Sci.* 39A (2008) 672–678.
- [24] S. Hanada, M. Ozeki, O. Izumi, Deformation characteristics in beta-phase Ti–Nb alloys, *Metall. Trans. A* 16 (1985) 789–795.
- [25] D.L. Moffat, U.R. Kattner, The stable and metastable Ti–Nb phase diagrams, *Metall. Trans. A* 19 (1988) 2389–2397.
- [26] M.J. Lai, C.C. Tasan, D. Raabe, Deformation mechanism of  $\omega$ -enriched Ti–Nb-based gum metal: dislocation channeling and deformation induced  $\omega$ – $\beta$  transformation, *Acta Mater.* 100 (2015) 290–300.
- [27] D.L. Moffat, D.C. Larbalestier, The competition between the alpha and omega phases in aged Ti–Nb alloys, *Metall. Trans. A* 19 (1988) 1687–1694.
- [28] D.L. Moffat, D.C. Larbalestier, The competition between martensite and omega in quenched Ti–Nb alloys, *Metall. Trans. A* 19 (1988) 1677–1686.
- [29] H.Y. Kim, Y. Ikehara, J.I. Kim, H. Hosoda, S. Miyazaki, Martensitic transformation, shape memory effect and superelasticity of Ti–Nb binary alloys, *Acta Mater.* 54 (2006) 2419–2429.
- [30] M. Tane, T. Nakano, S. Kuramoto, M. Niinomi, N. Takesue, H. Nakajima, Omega transformation in cold-worked Ti–Nb–Ta–Zr–O alloys with low body-centered cubic phase stability and its correlation with their elastic properties, *Acta Mater.* 61 (2013) 139–150.
- [31] J.-L. Zhang, L. Morsdorf, C.C. Tasan, Multi-probe microstructure tracking during heat treatment without an in-situ setup: case studies on martensitic steel, dual phase steel and  $\beta$ -Ti alloy, *Mater. Charact.* 111 (2016) 137–146.
- [32] A.P. Day, T.E. Quested, A comparison of grain imaging and measurement using horizontal orientation and colour orientation contrast imaging, electron backscatter pattern and optical methods, *J. Microsc.-Oxf* 195 (1999) 186–196.
- [33] L.A. Giannuzzi, F.A. Stevie (Eds.), *Introduction to Focused Ion Beams: Instrumentation, Theory, Techniques and Practice*, Springer, New York, 2005.
- [34] D. Yan, C.C. Tasan, D. Raabe, High resolution in situ mapping of microstrain and microstructure evolution reveals damage resistance criteria in dual phase steels, *Acta Mater.* 96 (2015) 399–409.
- [35] D. Raabe, K. Lücke, Rolling and annealing textures of BCC metals, in: H.J. Bunge (Ed.), *Proceedings of the 10th International Conference on Textures of Materials*, Pts 1 and 2-Icotom-10, vol. 157, Transtec Publications Ltd, Zurich-Uetikon, 1994, pp. 597–610.
- [36] B. Sander, D. Raabe, Texture inhomogeneity in a Ti–Nb-based beta-titanium alloy after warm rolling and recrystallization, *Mater. Sci. Eng. A-Struct. Mater. Prop. Microstruct. Process* 479 (2008) 236–247.
- [37] S.K. Sikka, Y.K. Vohra, R. Chidambaram, Omega-phase in materials, *Prog. Mater. Sci.* 27 (1982) 245–310.
- [38] S. Nag, R. Banerjee, R. Srinivasan, J.Y. Hwang, H.L. Fraser, omega-Assisted nucleation and growth of alpha precipitates in the Ti–5Al–5Mo–5V–3Cr–0.5Fe beta titanium alloy, *Acta Mater.* 57 (2009) 2136–2147.
- [39] S.J. Li, R. Yang, M. Niinomi, Y.L. Hao, Y.Y. Cui, Z.X. Gu, Phase transformation during aging and resulting mechanical properties of two Ti–Nb–Ta–Zr alloys, *Labour Hist. Rev.* 21 (2005) 678–686.



- [40] N. Sakaguchi, M. Niinomi, T. Akahori, J. Takeda, H. Toda, Relationships between tensile deformation behavior and microstructure in Ti-Nb-Ta-Zr system alloys, *Mater. Sci. Eng. C-Biomimetic Supramol. Syst.* 25 (2005) 363–369.
- [41] F.Q. Hou, S.J. Li, Y.L. Hao, R. Yang, Nonlinear elastic deformation behaviour of Ti-30Nb-12Zr alloys, *Scr. Mater.* 63 (2010) 54–57.
- [42] X.H. Min, K. Tsuzaki, S. Emura, K. Tsuchiya, Enhancement of uniform elongation in high strength Ti-Mo based alloys by combination of deformation modes, *Mater. Sci. Eng. A-Struct. Mater. Prop. Microstruct. Process* 528 (2011) 4569–4578.
- [43] R. Santhosh, M. Geetha, V.K. Saxena, M. Nageswararao, Studies on single and duplex aging of metastable beta titanium alloy Ti-15V-3Cr-3Al-3Sn, *J. Alloys Compd.* 605 (2014) 222–229.
- [44] W.D. Nix, H. Gao, Indentation size effects in crystalline materials: a law for strain gradient plasticity, *J. Mech. Phys. Solids* 46 (1998) 411–425.
- [45] J.-L. Zhang, S. Zaeferrer, D. Raabe, A study on the geometry of dislocation patterns in the surrounding of nanoindentations in a TWIP steel using electron channeling contrast imaging and discrete dislocation dynamics simulations, *Mater. Sci. Eng. A-Struct. Mater. Prop. Microstruct. Process* 636 (2015) 231–242.
- [46] D. Kuhlmann-wilsdorf, Theory of plastic deformation: properties of low energy dislocation structures, *Mater. Sci. Eng. A-Struct. Mater. Prop. Microstruct. Process* 113 (1989) 1–41.
- [47] I. Gutierrez-Urrutia, D. Raabe, Dislocation and twin substructure evolution during strain hardening of an Fe-22wt.%Mn-0.6wt.%C TWIP steel observed by electron channeling contrast imaging, *Acta Mater.* 59 (2011) 6449–6462.
- [48] E.O. Hall, The deformation and ageing of mild steel: III discussion of results, *Proc. Phys. Soc. Lond. Sect. B* 64 (1951) 747–753.
- [49] N.J. Petch, The cleavage strength of crystals, *J. Iron Steel Inst.* 174 (1953) 25–28.
- [50] I. Weiss, S.L. Semiatin, Thermomechanical processing of beta titanium alloys – an overview, *Mater. Sci. Eng. A-Struct. Mater. Prop. Microstruct. Process* 243 (1998) 46–65.
- [51] G. Lütjering, J.C. Williams, *Titanium*, Springer, Heidelberg, Germany, 2007.
- [52] M. Tane, T. Nakano, S. Kuramoto, M. Hara, M. Niinomi, N. Takesue, T. Yano, H. Nakajima, Low Young's modulus in Ti-Nb-Ta-Zr-O alloys: cold working and oxygen effects, *Acta Mater.* 59 (2011) 6975–6988.
- [53] L.S. Wei, H.Y. Kim, S. Miyazaki, Effects of oxygen concentration and phase stability on nano-domain structure and thermal expansion behavior of Ti-Nb-Zr-Ta-O alloys, *Acta Mater.* 100 (2015) 313–322.
- [54] Y. Zheng, R.E.A. Williams, S. Nag, R. Banerjee, H.L. Fraser, D. Banerjee, The effect of alloy composition on instabilities in the  $\beta$  phase of titanium alloys, *Scr. Mater.* 116 (2016) 49–52.
- [55] M. Kuzmina, M. Herbig, D. Ponge, S. Sandlöbes, D. Raabe, Linear complexes: confined chemical and structural states at dislocations, *Science* 349 (2015) 1080–1083.
- [56] M.M. Wang, C.C. Tasan, D. Ponge, A.C. Dippel, D. Raabe, Nanolaminate transformation-induced plasticity-twinning-induced plasticity steel with dynamic strain partitioning and enhanced damage resistance, *Acta Mater.* 85 (2015) 216–228.
- [57] M.M. Wang, C.C. Tasan, D. Ponge, D. Raabe, Spectral TRIP enables ductile 1.1 GPa martensite, *Acta Mater.* 111 (2016) 262–272.